Swift heavy ion irradiation induced magnetism in magnetically frustrated $BiMn_2O_5$ thin films

D. K. Shukla,[1,*] Ravi Kumar,[2] S. Mollah,[1] R. J. Choudhary,[3] P. Thakur,[4] S. K. Sharma,[5] N. B. Brookes,[4] and M. Knobel[5]
[1]*Department of Physics, Aligarh Muslim University, Aligarh 202002, India*
[2]*Centre for Materials Science and Engineering, National Institute of Technology, Hamirpur 177005, India*
[3]*UGC-DAE Consortium for Scientific Research, Indore 452001, India*
[4]*European Synchrotron Radiation Facility, BP 220, 38043 Grenoble Cedex, France*
[5]*Instituto de Fisica Gleb Wataghin, Universidade Estadual de Campinas (UNICAMP), Campinas 13.083-970, SP, Brazil*
(Received 18 May 2010; revised manuscript received 24 August 2010; published 23 November 2010)

The swift heavy ion (SHI) irradiation induces weak ferrimagnetism (FM) in magnetically frustrated polycrystalline $BiMn_2O_5$ thin films. This is manifested from irradiation induced higher energetic configuration that accounts for evolution of the Mn^{2+} state in the Mn^{3+}/Mn^{4+} network. Basically, this is the root of large magnetic moment in the irradiated samples. X-ray diffraction and Raman-scattering data of the samples indicate considerable modifications in the crystal structure after the SHI irradiation. FM in the irradiated samples and magnetically frustrated behavior of the pristine sample is apparent from dc magnetization measurements. Element specific characterizations such as near-edge x-ray absorption fine structure spectroscopy at O *K* and Mn $L_{3,2}$ edges along with x-ray magnetic circular dichroism at Mn $L_{3,2}$ edge show the evolution of the Mn^{2+} at disbursement of the Mn^{4+}. The microscopic origin behind the induced weak FM is found to be the increased orbital moment in the irradiated thin films.

DOI: 10.1103/PhysRevB.82.174432 PACS number(s): 77.55.Nv, 81.15.Gh, 61.80.Jh, 75.70.−i

I. INTRODUCTION

Field of multiferroics has created enormous curiosity among materials research communities and technologists during last few years.[1–21] Multiferroic materials exhibit concurrence of more than one ferroic properties (magnetic/ferroelectric/ferroelastic) in same phase, regardless of their contrasting origin, and offer the possibilities for variety of applications such as nonvolatile memories, capacitors, transducers, actuators, data storage multiple state memories, magnetic field sensors, etc.[1–9] Among recently discovered multiferroic materials, RMn_2O_5 (where R=rare earth, Y, and Bi) family demonstrates antiferromagnetism ($T_N \sim 39$ K) together with ferroelectricity ($T_C \sim 35$ K) and coupling between them which is a prerequisite for application purpose.[10–21] $BiMn_2O_5$ from above family has been studied widely,[12,15] whose magnetic structure is commensurate. It is ferroelectric at all temperatures below T_N and T_C with a propagation vector $q=(\frac{1}{2},0,\frac{1}{4})$. It is recently reported[14] that thin film of the $BiMn_2O_5$ is magnetically frustrated and its magnetic property is highly influenced by the strain. Fundamentally, thin films of the $BiMn_2O_5$ exhibit the magnetically frustrated spin-glass-type behavior, which is not acceptable for multiferroic applications.[14] This issue is an obstacle in realization of multiferroic-based memory devices of these materials. In fast moving technology of information storage system, chip-based memory and logic devices are imperative. Dependence on magnetic thin-film element for functionality and nonvolatile information storage will have added features due to simultaneous ferroelectricity. Recently, the remarkable pronouncements coming out of the ion beam treatment of magnetic materials (carried out on permalloy or CoPtCr, Fe-Pt, Ni-Fe, etc., having special relevance for application in magnetic information storage) have revealed the prospects to custom tailor the magnetic properties (e.g., moment, coercivity, anisotropy, magnetoresistance, etc.) which are crucial for application purposes.[22–25] The geometrical/magnetic structure of the $BiMn_2O_5$ offers various possibility of engineering its magnetic property by the ion beam.[12,16]

When swift heavy ion (SHI) passes through a material, it either excites or ionizes the atoms of the target by inelastic collisions or displaces them by elastic collisions. Elastic and inelastic collision processes are dominant, respectively, in the low- and high-energy regimes. It is evident from the literature that the electronic energy loss (S_e) owing to inelastic collision is capable of generating point/cluster defects if it is less than the threshold value of electronic energy loss (S_{eth}). If S_e is greater than S_{eth} (~ 14.25 keV/nm, for the present case), the energetic ions may create columnar amorphization. Stress/strain developed on account of the created defects or amorphization is responsible for the modification of the materials [Refs. 26–28 and references therein].

The present paper reports the 200 MeV Ag^{15+} ion irradiation induced weak ferrimagnetism (FM) in the magnetically frustrated polycrystalline $BiMn_2O_5$ thin films. Due to statistical nature of energy deposition process, stopping and range of ions in matter (SRIM) calculation[29] based on Monte Carlo simulation is used to plan the irradiation energy (~ 200 MeV). Consideration of ion fluences (1×10^{11}, 5×10^{11} and 1×10^{12} ions/cm^2) has been decided as an extended approximation of the single-ion impact.

II. EXPERIMENTAL DETAILS

Thin film of the $BiMn_2O_5$ (thickness ~ 200 nm) was deposited on *c*-axis-oriented single crystals of the $LaAlO_3$ (LAO) substrate by pulsed laser deposition (PLD) under optimized conditions using single phase target of the $BiMn_2O_5$ synthesized by solid state reaction route.[14,16] Thin film of the $BiMn_2O_5$ was cut into four pieces, each of 5×5 mm^2 size. In order to keep the growth conditions uniform for all the samples, these were used for irradiation and further studies.

 ©2010 The American Physical Society

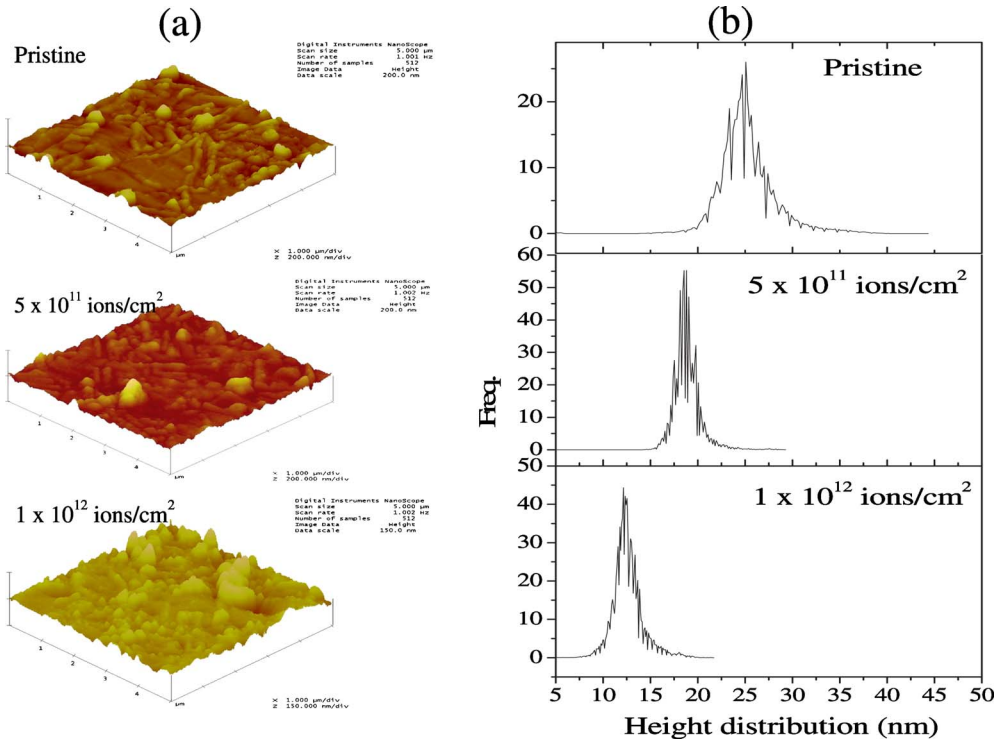

FIG. 1. (Color online) (a) AFM images of pristine as well as irradiated (with fluence values of 5×10^{11} and 1×10^{12} ions/cm^2) films; (b) Average height distribution obtained from 2D AFM images for pristine and irradiated thin films

One piece of the thin film was kept pristine while three other were irradiated with 200 MeV Ag^{15+} ion beam (at room temperature) using 15 UD Tandem Accelerator at Inter-University Accelerator Centre (IUAC), New Delhi, India, with different fluence values of the 1×10^{11}, 5×10^{11}, and 1×10^{12} ions/cm^2, respectively. The irradiation was performed under high-vacuum condition (base pressure 2×10^{-6} Torr). Incident angle of the ion beam was kept slightly away from surface normal of the sample to avoid the channeling effects. Beam current was kept very low (at 0.1 pnA) to avoid heating. The ion beam was uniformly scanned over 1 cm^2 area using a magnetic scanner. Fluence values were determined by measuring the charge falling over the sample surface under the secondary electron suppressed geometry. Ladder current was measured with a current integrator and a scalar counter. X-ray diffraction (XRD) measurement of the pristine as well as the irradiated thin films were carried out using Rigaku diffractometer with Cu $K\alpha$ radiation ($\lambda=1.54$ Å). Raman spectra were collected in back-scattering geometry utilizing a 10 mW Ar (488 nm) laser as an excitation source coupled with a Labram-HR800 micro-Raman spectrometer equipped with a 50× objective. Scattered light was analyzed with a Jobin Yvon Horiba LA-BRAM HR800 single monochromator and detected with a Peltier cooled charge-coupled device. Magnetic properties of the thin films were quantified through Quantum Design MPMS XL SQUID Magnetometer. Near-edge x-ray absorption fine structure (NEXAFS) at O K and Mn $L_{3,2}$ edges along with x-ray magnetic circular dichroism (XMCD) measurements at Mn $L_{3,2}$ edge were performed at the European Synchrotron Radiation Facility (ESRF) ID08 beamline. It uses an APPLE II type undulator to give ~100% linear/circular polarization. Base pressure of the experimental chamber was kept at $\sim3\times10^{-10}$ Torr. All the scans were collected simultaneously in total electron yield and total fluorescence yield modes, ensuring both surface and bulk sensitivities. Finally, the spectra were normalized to incident photon flux.

III. RESULTS AND DISCUSSION

Figure 1(a) shows the surface morphologies [atomic force microscopic (AFM) images] of the pristine and the irradiated (with fluence values 5×10^{11} and 1×10^{12} ions/cm^2) films at same scale (5 μm×5 μm). It is vivid from Fig. 1(a) that after irradiation, surfaces of the films adopt granular structures, and found to be more homogenized with increase in the irradiation fluence value. In order to directly visualize the effect of irradiation on the films' surface morphology, the height distribution profile of surfaces extracted from 2D AFM images are presented in Fig. 1(b). It shows decrease in the average height of grains and simultaneous increase in the frequency of average height with the enhancement of fluence values. Increase in frequency of average height distribution of grains is representative of the homogenized grain distribution after increase in the irradiation. Low frequency and relatively high average height of grains in pristine film correspond to the ridgeslike structure as reported earlier.[14]

Figure 2(a) displays the XRD pattern of the pristine and irradiated (with different fluence values of 1×10^{11}, 5×10^{11}, and 1×10^{12} ions/cm^2) thin films of the $BiMn_2O_5$ along with LAO substrate. All the peaks in case of pristine and irradiated thin films match either with those of bulk $BiMn_2O_5$ (Ref. 16) or with substrate, confirming the single

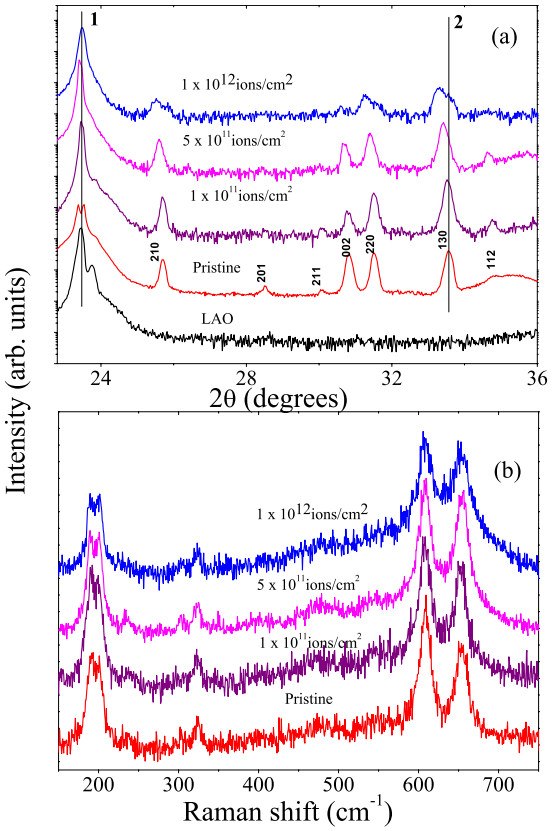

FIG. 2. (Color online) (a) XRD plots for pristine $BiMn_2O_5$/LAO thin film and irradiated with 1×10^{11}, 5×10^{11}, and 1×10^{12} ions/cm^2 fluence values; reference line 1 and 2 shows the substrate peak and one of the film peak, respectively. (b) Raman spectra for the same samples.

phase character of the samples even after irradiation. Since the lattice parameter of LAO substrate (a=3.789 Å) does not match closely with that of the $BiMn_2O_5$, its polycrystalline growth is ascertained. With increase in the irradiation dose, a shift in peak positions toward lower 2θ values is observed indicating augmentation in the lattice parameters. Two vertical reference lines (1 at substrate peak and 2 at one of the film peak) are drawn in the Fig. 2(a) for evident change in film peaks toward lower 2θ. Lattice parameters for the pristine as well as irradiated thin films have been calculated within orthorhombic symmetry (space group *Pbam*) and presented in the Table I. The lattice parameters of pristine film (Table I) are found to be different from those of bulk $BiMn_2O_5$ (a=7.5564 Å, b=8.5305 Å, and c =5.7589 Å). Evidently unit cell of pristine thin film is squeezed in two crystallographic directions hence considered to be strained along a axis. Direct effect of irradiation along a axis is observed even at the lowest fluence value (1×10^{11} ions/cm^2). Pristine thin film having strained structure along the a axis,[14] relaxes after the irradiation. Another important fact to be noticed is that with irradiation, the irradiated films' XRD peaks become broader than those of the pristine, which increases further with fluence values. Broadening of peak is due to formation of the smaller grain size with the irradiation. This observation is in agreement with the surface morphological behavior of the irradiated thin films observed in AFM images (Fig. 1). However distorted line shape and profile broadening of the XRD peaks for the maximum fluence (1×10^{12} ions/cm^2) indicate that subsequent increase in irradiation fluence may cause the amorphization.

TABLE I. Lattice parameters of pristine and irradiated (with 1×10^{11}, 5×10^{11}, and 1×10^{12} ions/cm^2) samples obtained from XRD data.

Sample	a (Å)	b (Å)	c (Å)
Pristine	7.5198	8.5694	5.8030
1×10^{11} ions/cm^2	7.5871	8.5695	5.8132
5×10^{11} ions/cm^2	7.6107	8.5942	5.8280
1×10^{12} ions/cm^2	7.6345	8.6190	5.8428

The lattice expansion in the irradiated films can be explained on the basis of energy deposition mechanism in the irradiation process. The above-mentioned findings demonstrate that the high electronic excitations have induced the structural modifications resembling nonmetallic systems.[30–33] Therefore, the S_e-dependent effects induced in these materials are probably related to the same basic energy transfer process between the incident ions and the target atoms, which can be explained using thermal spike model.[34,35] In this model, most of the energy of the incident ions is transferred to the host electrons during electronic slowing-down regime ($S_e \gg S_n$). This results in a huge increase in temperature of the electronic subsystem, far above its melting temperature. Nevertheless, this rapid heating is localized around the traveling ion path in the material and is followed by a rapid thermal quenching ($\sim10^{13}$–10^{14} K/s). Therefore, when the SHI passes through the $BiMn_2O_5$, rapid thermal quenching after massive heating may cause higher energetic configuration and consequent increase in the unit-cell volume. Above certain value, further increase in the fluence may cause a rapid increase in energy density, and the mean free path between displacing collisions approaches the interatomic spacing of the material.[36,37] At this stage, the subsequent thermal quenching may lead to the amorphized state. This is because the energy of Ag ion is 200 MeV, which corresponds to S_{eth} ($\sim$14.25 KeV/nm) of electronic energy loss as calculated by SRIM software.[29]

Considerable impact of the ion irradiation on the inertia of the structure is also observed from Raman spectroscopic data. Figure 2(b) demonstrates the Raman spectra for pristine and irradiated thin films. The site symmetry analysis[38] of the P*bam* structure of the $BiMn_2O_5$ yields a total 96 Γ-point phonon modes, out of which 48 phonon modes are Raman active ($\Gamma_{Raman}=13A_g+13B_{1g}+11B_{2g}+11B_{3g}$). By definition, the A_g modes are expected to appear in the parallel xx, yy, and zz scattering configuration and should not be observed in the crossed xy, yz, and zx configurations. However, the B_{1g}, B_{2g}, and B_{3g} modes are expected respectively in xy, xz, and yz configurations. Most of the predicted Raman modes have been identified, except a few, whose intensities are either very low or do not exist in the measured wave number range (150–700 cm^{-1}), this is consistent with the literature.[17,18] It

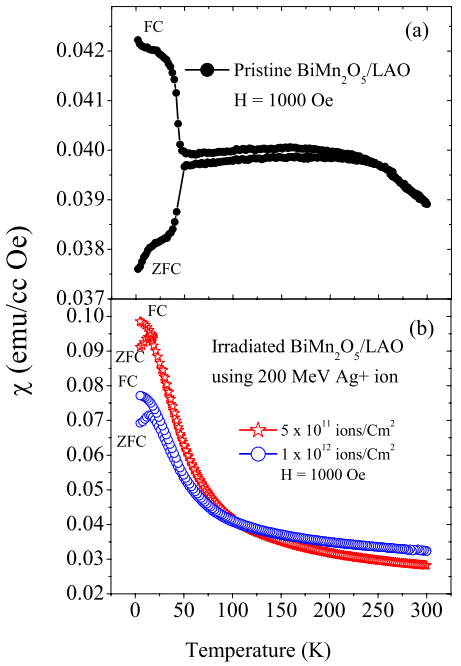

FIG. 3. (Color online) Magnetic susceptibility (χ) vs T plot measured at 1000 Oe in FC and ZFC cycle for (a) pristine $BiMn_2O_5$ thin film and (b) thin films irradiated with 5×10^{11} and 1×10^{12} ions/cm^2 fluence values.

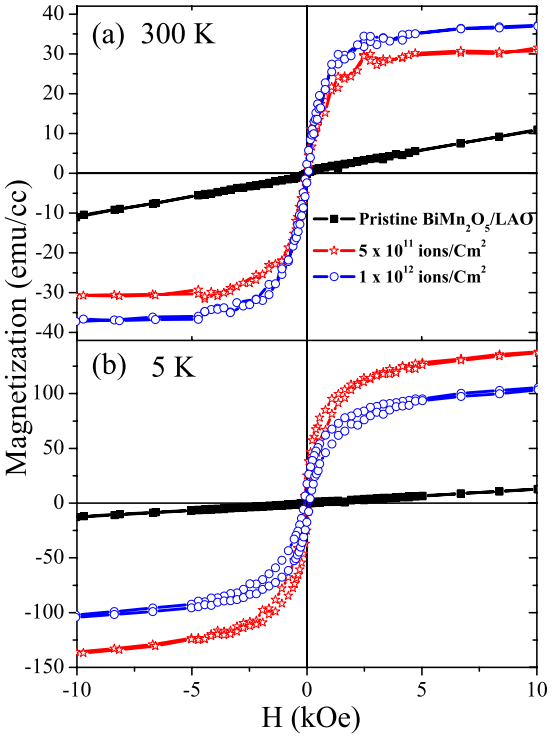

FIG. 4. (Color online) Magnetization (M) vs H plot for pristine $BiMn_2O_5$ thin film and thin films irradiated at 5×10^{11} and 1×10^{12} ions/cm^2 at (a) 300 K and (b) 5 K.

should be noted here that, as a result of substrate induced strain as seen in XRD data, modes in the pristine thin film are slightly shifted toward higher wave numbers (~3–5 nm) compared to those observed in the bulk $BiMn_2O_5$ (Ref. 39). Apparent peak broadening is observed in Raman spectra with increasing irradiation fluence which is the indicative of release of strain in the film, which is in conformity to the XRD data. Additionally, suppression in low waver-number modes with increasing fluence value is also observed indicating the increased electron-phonon coupling like superconductors.[40]

Modifications scrutinized in the structure of the irradiated thin films, as revealed by XRD and Raman spectra, would immensely affect the magnetic properties of the magnetically frustrated $BiMn_2O_5$. Thermal variation in zero-field-cooled (ZFC) and field-cooled (FC) magnetization in the presence of a magnetic field, $H=1000$ Oe for pristine and irradiated thin films (with fluence values 5×10^{11} and 1×10^{12} ions/cm^2) are shown in Figs. 3(a) and 3(b). It is evident from Fig. 3 that there is a clear contrast in the magnetization behaviors of the pristine and irradiated films. Pristine $BiMn_2O_5$ demonstrates a frustrated magnetic behavior as is obvious from its distinct FC and ZFC behavior. Moreover, M vs H curves (Fig. 4) at room temperature (300 K) and 5 K do not display any hysteresis in the pristine film as observed in bulk antiferromagnetic (AF) multiferroic $BiMn_2O_5$.[16] For pristine film, there is a broad region of nearly temperature-independent short-range order between 40 and 250 K. Above 250 K, the system enters smoothly into a paramagnetic state. Below 40 K, abrupt drop of magnetization in ZFC cycle and absence of any discernable magnetic loop at 5 K indicate low-temperature AF nature of the film. However, abrupt increase in magnetization below 40 K in FC cycle indicates the mixed phases of AF and FM in the film. Though we cannot infer the true ground state of the pristine film from these measurements, we may foresee the observed magnetic behavior arising due to complex magnetic structure of the $BiMn_2O_5$, having a competing ferromagnetic and antiferromagnetic exchange interactions.[14] It is known that bulk form of the sample exhibits AF transition at $T_N\sim40$ K. Nonetheless, substrate induced strain and other defects (such as oxygen vacancy) in thin films will further modify the different magnetic exchange interactions in the sample, giving rise to a frustrated magnetic behavior. In such situation, the protocol used for the magnetization measurements becomes crucial. AF like transition in ZFC at 40 K and abrupt increase in magnetization at the same temperature imply that there may be a kinetically arrested phase below this temperature, which are known to occur in several magnetically frustrated systems.[41,42] It should be noted here that the magnetic hysteresis measurement at 5 K in ZFC displays straight line without any hysteresis loop indicating AF like behavior. However, the MH curve measured at 5 K in FC mode shows a clear hysteresis loop (Fig. 5).

Surprisingly, the irradiation of the film with 200 MeV Ag^{15+} ions leads to a radical change in the magnetic phase of the material. It washes out the magnetically frustrated phase and stabilizes the weak ferrimagnetism [see Fig. 3(b)]. Temperature variation in inverse magnetic susceptibility ($1/\chi$) of the irradiated thin films (Fig. 6) shows an increase in the Curie-Weiss constant θ_{CW} (from −408 to −522 K) with increment of fluence values from 5×10^{11} to 1×10^{12} ions/cm^2. The θ_{CW} is obtained from intersecting

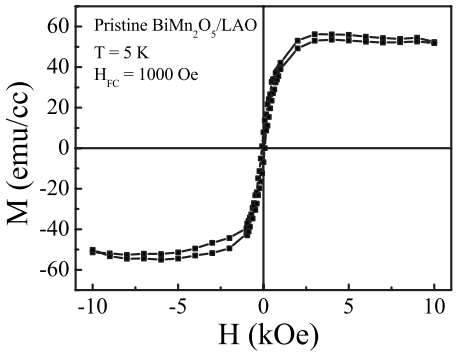

FIG. 5. Magnetization (M) vs H plot for pristine $BiMn_2O_5$ thin film at 5 K, measured after field cooling.

point of extrapolation of high-temperature region of $1/\chi$ vs T plots (Fig. 6). It represents the increase in negative molecular field and consequent increase in AF ordering of uncompensated spins. M vs H plots for irradiated samples at room temperature and 5 K compliment to the M vs T data, where hysteresis behavior for irradiated thin films is observed (Fig. 4). The induced weak ferrimagnetism after irradiation may be due to the inherent frustrated magnetic structure of the system. It is basically engineered by the irradiation induced modifications of the nearest-neighbor interactions (NNIs). Further, element specific characterizations such as NEXAFS and XMCD (discussed later) will help us to understand the effect of irradiation (observed change in the magnetic properties) in a quantitative way.

The geometrical structure of the $BiMn_2O_5$ consists of mixed valence Mn sites (Mn^{3+}/Mn^{4+}), where $Mn^{4+}O_6$ octahedra share edges to form infinite chains along the c axis. These chains are linked by pairs of $Mn^{3+}O_5$ pyramids and BiO_8 polyhedra. This exhibits five different NNI among Mn^{3+}/Mn^{4+} ions, which lead to the frustrated magnetic structure.[12,16] Various theoretical *ab initio* calculations and detailed analysis have been performed to understand the

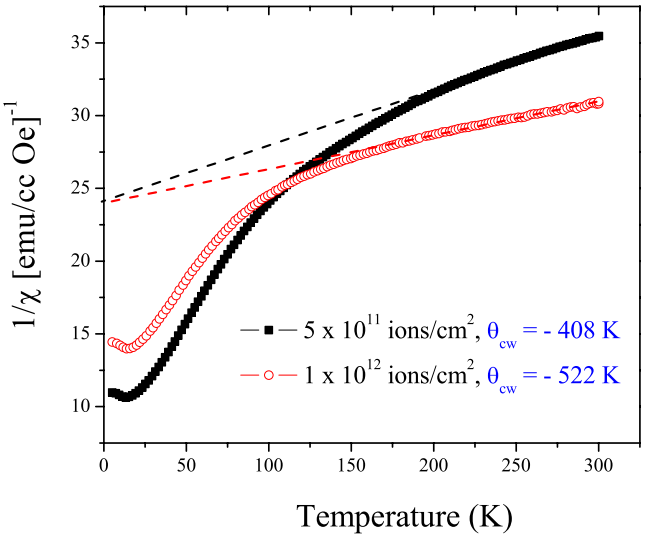

FIG. 6. (Color online) Inverse of magnetic susceptibility ($1/\chi$) vs T plot for $BiMn_2O_5$ thin films irradiated with 5×10^{11} and 1×10^{12} ions/cm^2 fluence values.

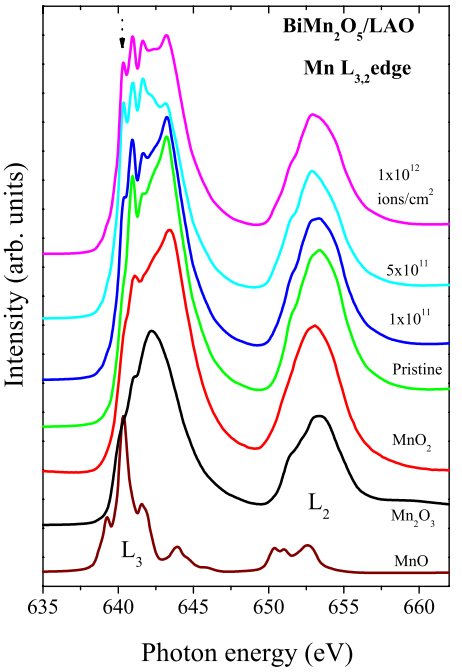

FIG. 7. (Color online) Normalized Mn $L_{3,2}$-edge NEXAFS spectra of pristine $BiMn_2O_5$ thin film and irradiated with 1×10^{11}, 5×10^{11}, and 1×10^{12} ions/cm^2 fluence values along with the spectra of MnO, Mn_2O_3, and MnO_2.

multiferroicity observed in RMn_2O_5. This suggests that $BiMn_2O_5$ exhibits a charge and spin ordering along the b direction, schematically denoted as a chain of $Mn^{3+}_{\uparrow}$-$Mn^{4+}_{\uparrow}$-$Mn^{3+}_{\downarrow}$. In the undistorted P*bam* structure, the distances $d_{\uparrow\uparrow}$(between $Mn^{3+}_{\uparrow}$ and $Mn^{4+}_{\uparrow}$) and $d_{\uparrow\downarrow}$ (between $Mn^{3+}_{\uparrow}$ and $Mn^{4+}_{\downarrow}$) are the same. But in the AF state ($T_N\sim39$ K), the $d_{\uparrow\uparrow}$ (between $Mn^{3+}_{\uparrow}$ and $Mn^{4+}_{\uparrow}$) is shortened and optimizes the double exchange interaction pioneering the ferroelectricity.[19–21] In the above scenario, the magnetic properties are very much susceptible to distances d between the Mn^{3+} and Mn^{4+} ions having strong U (~8 eV).[20] Therefore, a very high energetic impact would be required in order to disrupt the existing arrangement to justify the observed magnetic properties of irradiated films and recreate a new energetic configuration.

For Ag^{15+} projectile ion, the value of ionic energy corresponding to the maximum electronic energy loss in $BiMn_2O_5$ has been calculated to be 200 MeV, using SRIM.[29] When the 200 MeV Ag^{15+} ion passes though $BiMn_2O_5$, it produces an ion track of around 100 nm^2 cross-sectional area. Thus the number of ions required per square centimeter will be 1 cm^2/100 nm^2=1×10^{12}. Accordingly, the three fluences used in the irradiation experiment namely 1×10^{11}, 5×10^{11}, and 1×10^{12} ions/cm^2 are supposed to cover 10%, 50%, and 100% area, respectively. In order to check the accuracy of the above approximations (ion energy/ion fluences) in view of the induced weak ferrimagnetism, the microscopic observations are indispensable.

Figure 7 demonstrates the normalized Mn $L_{3,2}$-edge NEXAFS spectra of pristine and irradiated thin films along with the references MnO (Mn2+), Mn_2O_3 (Mn3+), and MnO_2 (Mn4+), collected at room temperature. The spin-orbit inter-

action of the Mn $2p$ core states splits these spectra into two broad multiplets, namely, L_3 $(2p_{3/2})$ and L_2 $(2p_{1/2})$ with an energy ~11 eV apart. Each of these two regions further split into t_{2g} and e_g orbital features because of the crystal-field effect of neighboring ions. These spectra illustrate the valence-specific multiplet structure with a chemical shift due to change in the oxidation state. The inflection point of Mn L_3 edge shifts toward the higher energy as the valence number of Mn increases from +2 in MnO to +4 in MnO_2. The Mn $L_{3,2}$ NEXAFS spectrum of pristine and irradiated thin films can be directly compared with the reference compounds on the basis of peak positions. In pristine thin film, Mn ions are found to be in the $Mn^{+3.5}$ state as the ratio of Mn^{3+}/Mn^{4+} is 1 in the $BiMn_2O_5$. Detailed description of Mn $L_{3,2}$ NEXAFS spectra of pristine thin film with references are presented in our earlier work.[14] As a focus of the presented work, the SHI irradiation induced modifications in Mn charge states can be directly observed in both L_3 and L_2 peaks, with more in L_3 edges since it is more susceptible to local environment than L_2. After irradiation even with lowest fluence $(1\times10^{11}$ ions/cm$^2)$, the L_3 region shows an evolution of new peak at ~640 eV (marked by an arrow). This exactly matches with the intense L_3 peak of MnO which has the domination of t_{2g} states, indicating that some part of Mn ions are transferred into Mn^{2+}. It leads to the change in the ratio Mn^{3+}/Mn^{4+} of pristine film from 1.

With evolution of the Mn^{2+}, peak at ~643 eV (signature of the Mn^{4+}) diminishes, confirming that evolution of the Mn^{2+} at the expense of Mn^{4+}. In this scenario, the spectral signature of Mn^{3+}, which is left undistributed, will have more obvious dominancy in this multiplet spectrum and is clearly observed at ~641.5 eV. Shift in L_2 peak toward lower energy also vindicates the increased spectral weightage of Mn^{3+}. For further increased irradiation fluence value, L_3 region follows the trend of spectral distribution of multiplet structure among $Mn^{2+}/Mn^{3+}/Mn^{4+}$ in accordance with the approximation of fluence values covering surface area. Noticeably, for the maximum fluence value $(1\times10^{12}$ ions/cm$^2)$, the spectrum does not follow the above approximation and gives an idea about the random crystal-field effect in spectrum. It is evidenced by the decreased crystallinity of this sample from the XRD pattern [see Fig. 2(a)]. Increased value of the Mn^{2+} content at the expense of Mn^{4+} with increase in the irradiation fluence may be accepted as a direct consequence of increasing magnetic moment. However, in order to acquire the in-depth information about magnetic contribution from the Mn^{2+}, XMCD is performed at 100 and 300 K.

Well established XMCD method is one of the most reliable techniques for directly measuring the magnetic moments in a valence shell. Figure 8 demonstrates the normalized XMCD spectra measured at a magnetic field of 5 T for (a) the pristine thin film and (b) irradiated with fluence value of 5×10^{11} ions/cm^2. Although there is a little dependence of the NEXAFS signal on the polarization of the incident x-ray photon, there is a clear reproducible difference between the NEXAFS collected for the photon helicity parallel and antiparallel with the applied magnetic field (5 T), which is the XMCD signal. Lower parts of Fig. 8 show the XMCD spectra of the respective sample at 300 and 100 K. In the

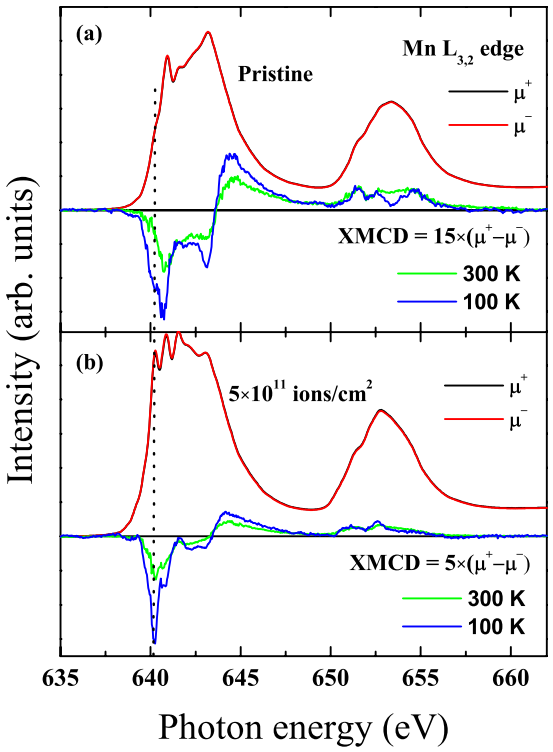

FIG. 8. (Color online) Mn $L_{3,2}$ edge XMCD spectra at 100 and 300 K for pristine $BiMn_2O_5$ thin film and one irradiated with fluence value of 5×10^{11} ions/cm^2.

XMCD spectra for all the irradiated samples, (though presented here for only one irradiated sample) the XMCD signal of Mn^{2+} at energy ~640 eV is clearly observed, which is in accordance with the spectral position of the Mn^{2+} observed in NEXAFS spectra (Fig. 7) for irradiated samples. It is also to be pointed out that the XMCD signal of the Mn^{2+} increases with the increase in fluence value and is higher at lower temperatures. The temperature dependence of XMCD signal of the Mn^{2+} indicates the paramagnetic contribution toward the magnetism of the system. The x-ray absorption sum rule suggests that the total intensity of the L_3 and L_2 resonates with the number n_h of empty d states (holes). For a magnetic material, the d shell has a spin magnetic moment which is given by the imbalance of spin-up and spin-down electrons or equivalently by the imbalance of spin-up and spin-down holes. The use of right or left circularly polarized photons, which transfer their angular momentum to the excited photoelectrons, measure the difference in the number of d holes. Evolution of the Mn^{2+} changes the d holes' contribution (n_h=5, 6, and 7 for Mn^{2+}, Mn^{3+}, and Mn^{4+}, respectively) and consequently affect the XMCD spectra. In order to separate out the contributions from spin as well as orbital part of the total magnetic moment, sum rules have been utilized.[43] According to sum rules, expressions of orbital magnetic moment $\langle L_Z\rangle$, and spin magnetic moment $\langle S_Z\rangle$, are written as

$$\langle L_Z\rangle = \frac{2(A+B)}{3C} n_h \tag{1}$$

TABLE II. Orbital (L_z) and spin (S_z) magnetic moments (in μ_B) calculated from XMCD data of pristine and thin film irradiated with the fluence value 5×10^{11} ions/cm^2 at 100 and 300 K by using sum rule.

	100 K		300 K	
Sample	L_Z	S_Z	L_Z	S_Z
Pristine	-2.4588×10^{-5}	-3.60663×10^{-3}	3.24123×10^{-3}	-5.28374×10^{-3}
5×10^{11} ions/cm^2	-7.40033×10^{-4}	-2.9393×10^{-3}	1.88051×10^{-3}	-5.169499×10^{-3}

$$\langle S_Z\rangle = \frac{(A-2B)}{2C} n_h \tag{2}$$

where A and B are the areas of the L_3 and L_2 edges, respectively, in the XMCD difference spectra. C is the area under the $L_{3,2}$-edge NEXAFS spectra and n_h is the number of holes in the $3d$ orbital of Mn ions. Here we have neglected the spin-quadrupole coupling term $\langle T_Z\rangle$. The sum rules have been tested by comparison with the experimental measurements and theoretical calculations[44] which are generally accurate within 10% error. One possible source of error is found for the early transition metals, such as Cr, where the multiplet effects are larger than the $2p$ spin-orbit coupling and hence the L_2 and L_3 edges cannot be separated. However, it is not the case here. Value of n_h used in the above formula is 6.5 for pristine sample (as Mn^{3+}/Mn^{4+} ratio equals to 1) and 6 for irradiated with fluence 5×10^{11} ions/cm^2 (assuming 50% of Mn^{4+} are transferred into Mn^{2+}). To address the irradiation-induced effect separately on L_Z and S_Z, the temperature-dependent values for sample irradiated by intermediate fluence (5×10^{11} ions/cm^2) and the pristine one are compared in Table II. Room-temperature values of L_Z and S_Z bearing opposite sign indicate the canceling nature of the orbital and spin magnetic moments. However, the calculated values at low temperature designate the summing nature in both the samples. The most noticeable parameter in this calculation is the value of orbital magnetic moment, which seems to have larger impact on total magnetic moment.

The orbital magnetic moment contribution to the XMCD spectrum can be obtained from the ratio (R) of L_2 and L_3 peak areas.[45] For $R\sim-1$, the orbital magnetic moment is practically quenched and increases with the increasing deviation from this value. Notable difference in R for pristine and irradiated samples can be clearly seen in the corresponding XMCD spectra (Fig. 8). This evidences a large orbital contribution to the magnetic moment in irradiated samples. $L_{2,3}$-peak areas have been extracted from the XMCD signal for the pristine and 5×10^{11} ions/cm^2 fluence irradiated samples for quantitative evaluation of the orbital (μ_l) to spin (μ_s^{eff}) magnetic moment ratio according to the formula (see Table III)

$$\frac{\mu_l}{\mu_s^{eff}} = \frac{2}{3}\frac{(1+R)}{(1-2R)}. \tag{3}$$

The ratio of orbital to spin magnetic moment indicates the relative strength of orbital magnetism. The result obtained from the sum rule and orbital magnetic moment calculation is found to be in well agreement with each other. If one follows both the results together (Table III), analysis can be summarized as: (i) at room temperature, the orbital magnetic moment in pristine sample is more than the irradiated one but the total observed magnetic moment is less because of around equally opposite spin magnetic moment. However, it is not the case in irradiated sample where we do observe the consequences of spin magnetic moment. (ii) at 100 K, the orbital magnetic moment in the pristine sample is almost quenched ($R\sim-1$) and the resultant AF is due to spin magnetic moment only. While in the irradiated sample, contribution of orbital magnetic moment is increased. Finally, the XMCD spectra (Fig. 8) evidences to the microscopic behavior of weak ferrimagnetism induced in to the system after irradiation. These results are in good agreement to the dc magnetization data (Figs. 4 and 5).

It is important to mention that the Mn^{2+} does not carry any orbital magnetic moment. But along with the evolution of Mn^{2+} state, the observation of orbital magnetic moment obtained from the calculation of XMCD data using well established sum rules indicate to have more complicated magnetic network of $Mn^{2+}/Mn^{3+}/Mn^{4+}$. In the present article, a quantitative analysis of $Mn^{2+}/Mn^{3+}/Mn^{4+}$ is not performed. Nevertheless, as a possible explanation for increasing orbital moment, one may suspect to have varying ratio of Mn^{3+}/Mn^{4+} due to change in the Bi ion valency. If we consider this scenario, Bi exists either in III or V oxidation states only. And in both of these oxidation states it can form octahedra with 6 coordination numbers. It is to be noticed here that in V state, Bi has much lower ionic radii (0.09 nm) than in III state (0.117 nm). Because of continuous increment in the unit-cell size with the increasing fluence value (Table I), Bi V state is ruled out. Another fact to prolong this discussion may be NEXAFS spectra of O K edge (Fig. 9), explained in next section, which also supports that the Bi valency remains unchanged. In this situation, on the basis of proofs available, the complex magnetic network of

TABLE III. Experimental value of R (ratio of L_2 and L_3 peak areas) and derived orbital/spin magnetic moment ratios for pristine and thin film irradiated with the fluence value 5×10^{11} ions/cm^2, at 100 and 300 K.

	100 K		300 K	
Sample	R	μ_l/μ_s^{eff}	R	μ_l/μ_s^{eff}
Pristine	−0.98	0.0044	−18.28	−0.3067
5×10^{11} ions/cm^2	−0.58	0.1296	−2.80	−0.1818

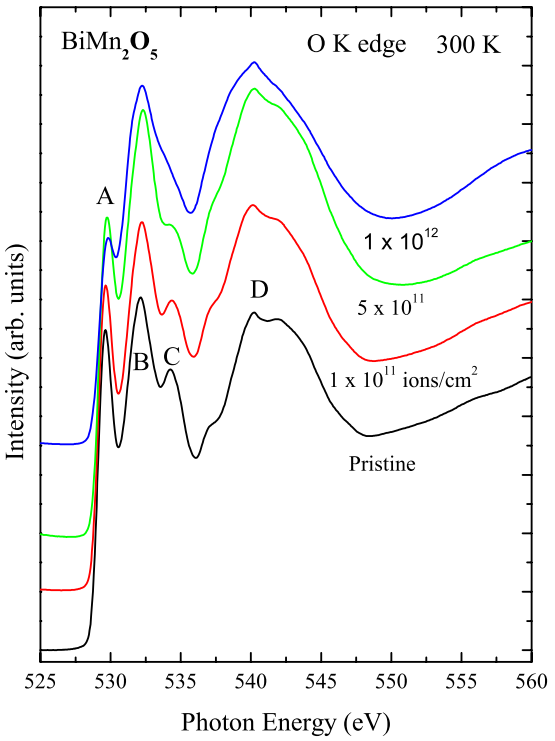

FIG. 9. (Color online) Normalized O *K*-edge NEXAFS spectra of pristine $BiMn_2O_5$ thin film and irradiated with 1×10^{11}, 5×10^{11}, and 1×10^{12} ions/cm^2 fluence values at 300 K.

$Mn^{2+}/Mn^{3+}/Mn^{4+}$ is attributed to the observed orbital magnetic moment. Here, it is proposed that magnetic structure solving techniques like neutron diffraction may be performed on this compound for better understanding.

In present case, we observe the irradiation induced evolution of the Mn^{2+} and consequently the major changes in hybridization and crystal-field symmetry in Mn $L_{3,2}$ NEXAFS spectra. Important supporting facts may be drawn from O *K* edge. Figure 9 shows the normalized O *K*-edge NEXAFS spectra of the pristine and irradiated samples collected at room temperature. It arises mainly due to the transition of O 1*s* electron to the conduction band near the Fermi surface, which is dominated by the hybridization of metal 3*d* and Bi 6*s* and 6*p* orbitals with the O 2*p* orbitals. Hence, it provides the reasonable estimate of the unoccupied conduction bands.[46] The comparison of O *K*-edge NEXAFS spectra of pristine thin film with those of MnO, MnO_2 and Bi_2O_3 has been presented elsewhere.[14] In O *K*-edge spectra, four main features are leveled as A, B, C, and D in the energy range from 528 to 545 eV. The first two spectral features (A and B) which form the bottom of the conduction band are attributed to transitions from 1*s* core state to oxygen 2*p* states hybridized with mixed-valent Mn 3*d* orbitals. The exact assignment of these pre-edge features is still not clear and has been discussed controversially in literature [see Ref. 47 and references therein]. With the increase in irradiation fluence value, the concurrence decrease in the peak A is observed, whereas peak B remains unchanged. This inspection is in confirmation to the fact that in fixed amount of mixed valent Mn ion states (Mn^{3+}/Mn^{4+}), the irradiation-induced evolution of Mn^{2+} will cause the decrease in unoccupancies of *d* shell (or we may say an increase in the density of states related to Mn ions). Peaks C and D are identified to be due to the hybridization between O 2*p*-Bi 6*s* orbitals with small admixture of Mn 3*d* e_g minority spin states and O 2*p*-(Bi 6*p*+Mn 4*sp*) orbitals, respectively. Peak D is broader than others, which explains that unoccupancies are not in the specified subbands. The properties of peak C at 533 eV depends upon the behavior of highly polarizable $6s^2$ lone pair of Bi^{3+} ion. Interestingly, spectral features of the peak C remains unchanged up to the irradiation fluence value 5×10^{11} ions/cm^2. Therefore, one may expect the existence of ferroelectricity up to this fluence value in the presence of irradiation-induced FM. This could not be measured as the substrate (LAO) is nonconducting.

IV. CONCLUSIONS

In conclusion, a model irradiation experiment has been performed using 200 MeV Ag^{15+} ion as projectile and magnetically frustrated PLD grown thin film of the multiferroic $BiMn_2O_5$ as a target. With increasing irradiation fluence, an isotropic increase in the unit-cell parameters and simultaneous decrease in grain size in primarily strained structure is observed. This may be due to the consequence of new higher energetic configuration after irradiation. Interestingly, irradiation induced onset of weak ferrimagnetism is observed in a magnetically frustrated system. Element-specific observations using NEXAFS and XMCD show the evolution of Mn^{2+} in a network of Mn^{3+}/Mn^{4+} at the expense of Mn^{4+}. These findings spur that the SHI irradiation may be used to custom-tailor the properties of oxide multiferroics for technological applications.

ACKNOWLEDGMENTS

D.K.S. is thankful to CSIR, New Delhi, India for providing financial support. Authors are thankful to V. G. Sathe for help in Raman measurements at UGC-CSR, Indore. Department of Science and Technology (DST), Government of India, is acknowledged for supporting this work under Project No. S2/SR/CMP-0051/2007. Two of the authors (S.K.S. and M.K.) are very grateful to FAPESP and CNPq (Brazil) for affording financial support.

*Present address: Deutsches Elektronen-Synchrotron (DESY), Notkestrasse 85, Hamburg 22603, Germany; shukladk@gmail.com

[1] Ce-Wen Nan, M. I. Bichurin, Shuxiang Dong, D. Viehland, and G. Srinivasan, J. Appl. Phys. **103**, 031101 (2008).
[2] S. H. Baek, H. W. Jang, C. M. Folkman, Y. L. Li, B. Winchester, J. X. Zhang, Q. He, Y. H. Chu, C. T. Nelson, M. S. Rzchowski, X. Q. Pan, R. Ramesh, L. Q. Chen, and C. B. Eom, Nature Mater. **9**, 309 (2010).
[3] D. Lebeugle, A. Mougin, M. Viret, D. Colson, and L. Ranno, Phys. Rev. Lett. **103**, 257601 (2009).
[4] N. E. Rajeevan, P. P. Pradyumnan, R. Kumar, D. K. Shukla, S. Kumar, A. K. Singh, S. Patnaik, S. K. Arora, and I. V. Shvets, Appl. Phys. Lett. **92**, 102910 (2008).
[5] R. Ramesh and N. A. Spaldin, Nature Mater. **6**, 21 (2007).
[6] W. Eerenstein, N. D. Mathur, and J. F. Scott, Nature (London) **442**, 759 (2006).
[7] M. Gajek, M. Bibes, S. Fusil, K. Bouzehouane, J. Fontcuberta, A. Barthélémy, and A. Fert, Nature Mater. **6**, 296 (2007).
[8] S. W. Cheong and M. Mostovoy, Nature Mater. **6**, 13 (2007).
[9] N. Hur, S. Park, P. A. Sharma, J. Ahn, S. Guha, and S. W. Cheong, Nature (London) **429**, 392 (2004).
[10] D. K. Shukla, Ravi Kumar, S. Mollah, R. J. Choudhary, P. Thakur, S. K. Sharma, N. B. Brookes, and M. Knobel, J. Appl. Phys. **107**, 09D903 (2010).
[11] L. C. Chapon, P. G. Radaelli, G. R. Blake, S. Park, and S. W. Cheong, Phys. Rev. Lett. **96**, 097601 (2006).
[12] A. Muñoz, J. A. Alonso, M. T. Casais, M. J. Martinez-Lope, J. L. Martinez, and M. T. Fernandez-Diaz, Phys. Rev. B **65**, 144423 (2002).
[13] G. R. Blake, L. C. Chapon, P. G. Radaelli, S. Park, N. Hur, S.-W. Cheong, and J. Rodríguez-Carvajal, Phys. Rev. B **71**, 214402 (2005).
[14] D. K. Shukla, R. Kumar, S. K. Sharma, P. Thakur, R. J. Choudhary, S. Mollah, N. B. Brookes, M. Knobel, K. H. Chae, and W. K. Choi, J. Phys. D **42**, 125304 (2009).
[15] C. Vecchini, L. C. Chapon, P. J. Brown, T. Chatterji, S. Park, S.-W. Cheong, and P. G. Radaelli, Phys. Rev. B **77**, 134434 (2008).
[16] D. K. Shukla, S. Mollah, R. Kumar, P. Thakur, K. H. Chae, A. Banerjee, and W. K. Choi, J. Appl. Phys. **104**, 033707 (2008).
[17] B. Mihailova, M. M. Gospodinov, B. Güttler, F. Yen, A. P. Litvinchuk, and M. N. Iliev, Phys. Rev. B **71**, 172301 (2005).
[18] A. F. García-Flores, E. Granado, H. Martinho, R. R. Urbano, C. Rettori, E. I. Golovenchits, V. A. Sanina, S. B. Oseroff, S. Park, and S. W. Cheong, Phys. Rev. B **73**, 104411 (2006).
[19] C. Wang, G. C. Guo, and L. He, Phys. Rev. Lett. **99**, 177202 (2007).
[20] G. Giovannetti and J. van den Brink, Phys. Rev. Lett. **100**, 227603 (2008).
[21] D. V. Efremov, J. van den Brink, and D. I. Khomskii, Nature Mater. **3**, 853 (2004).
[22] R. Allenspach, A. Bischof, U. Dürig, and P. Grütter, Appl. Phys. Lett. **73**, 3598 (1998).
[23] G. S. Chang, T. A. Callcott, G. P. Zhang, G. T. Woods, S. H. Kim, S. W. Shin, K. Jeong, C. N. Whang, and A. Moewes, Appl. Phys. Lett. **81**, 3016 (2002).
[24] O. Hellwig, D. Weller, A. J. Kellock, J. E. E. Baglin, and E. E. Fullerton, Appl. Phys. Lett. **79**, 1151 (2001).
[25] S. Maat, A. J. Kellock, D. Weller, J. E. E. Baglin, and E. E. Fullerton, J. Magn. Magn. Mater. **265**, 1 (2003).
[26] C. Houpert, F. Studer, D. Groult, and M. Toulmonde, Nucl. Instrum. Methods Phys. Res. B **39**, 720 (1989).
[27] R. Kumar, S. B. Samantra, S. K. Arora, A. Gupta, D. Kanjilal, R. Pinto, and A. V. Narlikar, Solid State Commun. **106**, 805 (1998).
[28] R. Kumar, S. K. Arora, D. Kanjilal, G. K. Mehta, R. Bache, S. K. Date, S. R. Shinde, L. V. Saraf, S. B. Ogale, and S. I. Patil, Radiat. Eff. Defects Solids **147**, 187 (1999).
[29] J. P. Biersack and L. G. Haggmark, Nucl. Instrum. Methods Phys. Res. **174**, 257 (1980).
[30] Z. G. Wang, C. Dufour, E. Paumier, and M. Toulemonde, J. Phys.: Condens. Matter **6**, 6733 (1994).
[31] K. Izui and S. Furuno, *Proceedings of the 11th International Congress on Electron Microscopy*, Kyoto 1986, edited by T Imura, S. Maruse, and T Suzuki (Japan Society of Electron Microscopy, Tokyo, 1986), p 1299.
[32] A. Meftah, F. Brisard, J. M. Costantini, M. Hage-Ali, J. P. Stoquert, F. Studer, and M. Toulemonde, Phys. Rev. B **48**, 920 (1993).
[33] F. Thibaudau, J. Cousty, E. Balanzat, and S. Bouffard, Phys. Rev. Lett. **67**, 1582 (1991).
[34] M. Toulemonde, Nucl. Instrum. Methods Phys. Res. B **156**, 1 (1999).
[35] M. Toulemonde, C. Dufour, and E. Paumier, Phys. Rev. B **46**, 14362 (1992).
[36] J. A. Brinkman, J. Appl. Phys. **25**, 961 (1954).
[37] J. A. Brinkman, Am. J. Phys. **24**, 246 (1956).
[38] D. L. Rousseau, R. P. Bauman, and S. P. S. Porto, J. Raman Spectrosc. **10**, 253 (1981).
[39] D. K. Shukla *et al.*, J. Phys.: Condens. Matter **22**, 485901 (2010).
[40] M. N. Iliev, V. G. Hadjiev, S. Jandl, D. Le Boeuf, V. N. Popov, D. Bonn, R. Liang, and W. N. Hardy, Phys. Rev. B **77**, 174302 (2008).
[41] G. C. Milward, M. J. Calderon, and P. B. Littlewood, Nature (London) **433**, 607 (2005).
[42] P. Chaddah, K. Kumar, and A. Banerjee, Phys. Rev. B **77**, 100402(R) (2008).
[43] P. Carra, B. T. Thole, M. Altarelli, and X. Wang, Phys. Rev. Lett. **70**, 694 (1993).
[44] T. Funk, A. Deb, Simon J. George, H. Wang, and S. P. Cramer, Coord. Chem. Rev. **249**, 3 (2005).
[45] W. D. Brewer, A. Scherz, C. Sorg, H. Wende, K. Baberschke, P. Bencok, and S. Frota-Pessôa, Phys. Rev. Lett. **93**, 077205 (2004).
[46] F. M. F. de Groot, M. Grioni, J. C. Fuggle, J. Ghijsen, G. A. Sawatzky, and H. Petersen, Phys. Rev. B **40**, 5715 (1989).
[47] N. Mannella, A. Rosenhahn, M. Watanabe, B. Sell, A. Nambu, S. Ritchey, E. Arenholz, A. Young, Y. Tomioka, and C. S. Fadley, Phys. Rev. B **71**, 125117 (2005).